A Comprehensive Compact-Modeling Methodology for Spiral Inductors in Silicon-Based RFICs

Adam C. Watson, *Student Member, IEEE*, Daniel Melendy, *Member, IEEE*, Pascale Francis, Kyuwoon Hwang, and Andreas Weisshaar, *Senior Member, IEEE*

***Abstract*—A new comprehensive wide-band compact-modeling methodology for on-chip spiral inductors is presented. The new modeling methodology creates an equivalent-circuit model consisting of frequency-independent circuit elements. A fast automated extraction procedure is developed for determining the circuit element values from two-port S-parameter measurement data. The methodology is extremely flexible in allowing for accurate modeling of general classes of spiral inductors on high- or low-resistivity substrate and for large spirals exhibiting distributed trends. The new modeling methodology is applied to general classes of spirals with various sizes and substrate parameters. The extracted models show excellent agreement with the measured data sets over the frequency range of 0.1–10 GHz.**

***Index Terms*—Distributed effects, equivalent-circuit model, integrated passives, proximity effect, RF integrated circuit (RFIC), silicon, skin effect, spiral inductors, substrate eddy currents.**

I. Introduction

SINCE ITS introduction, the integrated circuit (IC) has pervaded nearly every aspect of modern life. Recently, there has been increased emphasis on RF and mixed-signal ICs, including the creation of system on chip (SoC). A particularly difficult aspect in the integration process is the embedding of passives, such as planar spiral inductors, as illustrated in Fig. 1. However, despite the difficulties, the benefits of embedding passives on-chip are substantial, including significant increases in reliability and performance of the IC combined with lower cost [1]. As a result, the use of monolithically integrated on-chip spiral inductors has become commonplace in the IC industry.

The RF and mixed-signal IC design process requires accurate inductor models that can be included in the circuit simulation along with the entire IC design. The implemented inductor model should be composed of frequency-independent circuit elements to allow for time-domain circuit simulation in common circuit simulators such as SPICE. To give the IC design engineers a real benefit, the compact-model topology should use a minimum number of ideal lumped elements while offering a maximum amount of modeling flexibility. Furthermore, having a robust automated extraction procedure is desirable to reliably and quickly produce circuit models for a given spiral inductor design on demand.

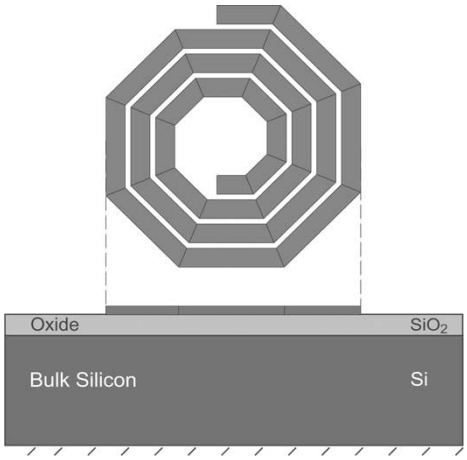

Fig. 1. Planar spiral inductor on silicon substrate.

The most commonly used compact spiral inductor model is the standard "nine-element" π-model (e.g., [2] and [3]). The series branch of the nine-element model consists of a series combination of an inductor and a resistor together with a parallel-connected capacitor, which may be thought of as representing the capacitive coupling to the underpass, as well as between the turns of the spiral inductor. While this model is useful over a limited frequency range for electrically small spiral inductors on low-loss substrates, it does not properly model distributed effects as well as higher order loss effects, including conductor skin and proximity effects in the metallization and eddy-current loss in the silicon substrate for heavily doped silicon processes. The lack of a single accurate wide-band model typically leads to the creation of many narrow-band models for a given spiral inductor. The problem of producing multiple narrow-band models is compounded by the availability of many different spiral inductors for a given silicon process. A wide-band modeling approach significantly simplifies this bottleneck in the design flow by providing a single model for a given spiral inductor. A wide-band spiral inductor model also has the capability of providing a valuable accurate response outside the main frequency band of interest for a specific application.

This paper presents a new comprehensive methodology for wide-band compact modeling of on-chip spiral inductors, including automated component value extraction. The proposed wide-band models consist entirely of ideal lumped elements to make them compatible for transient analysis in common circuit simulators. In order to make the models wide-band, two

Manuscript received April 18, 2003; revised August 19, 2003.

A. C. Watson and A. Weisshaar are with the School of Electrical Engineering and Computer Science, Oregon State University, Corvallis, OR 97331-3211 USA (e-mail: andreas@eecs.oregonstate.edu).

D. Melendy was with the Department of Electrical Engineering and Computer Science, Oregon State University, Corvallis, OR 97331-3211 USA. He is now with the National Semiconductor Corporation, Federal Way, WA 98001 USA.

P. Francis and K. Hwang are with the National Semiconductor Corporation, Santa Clara, CA 95052 USA.

Digital Object Identifier 10.1109/TMTT.2004.823594

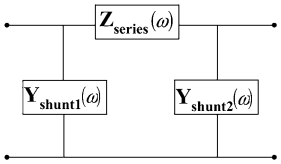

Fig. 2. Standard single-π network topology for compact spiral inductor models.

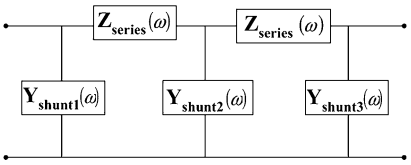

Fig. 3. Distributed double-π network topology.

major frequency-dependent effects are included. These are frequency-dependent series loss in the metallization and lossy substrate, as well as distributed effects.

Frequency-dependent series loss in the spiral inductor is modeled using transformer loops (similar to the substrate current loops used in the equivalent-circuit models for on-chip interconnects [4], [5]). A simple transformer structure has also recently been used for scalable modeling of spiral inductors [6]. The single-π model augmented with transformer loops to incorporate the effects of frequency-dependent series loss in spiral inductors achieves high accuracy over a wide frequency range, in particular, for spiral inductors on low-resistivity substrates, where eddy-current loss in the substrate is dominant [8], [9].

The limitations of the single-π network topology (Fig. 2) become apparent as the physical size of the spiral becomes electrically larger. Distributed effects in spiral inductors are directly observed as a decrease in the *effective* series branch resistance $R_{12}(\omega)$ at higher frequencies, even to negative values in the frequency-range of interest, where the series branch impedance is given by

$$Z_{\text{series}}(\omega) = -\frac{1}{Y_{12}(\omega)} = R_{12}(\omega) + j\omega L_{12}(\omega) \qquad (1)$$

and $Y_{12}(\omega)$ is the mutual short-circuit admittance parameter of the two-port network. The decrease in $R_{12}(\omega)$ cannot be represented by the one-port branch series impedance element $Z_{\text{series}}(\omega)$ in Fig. 2 consisting of only ideal lumped R, L, C elements. In order to represent these distributed effects, a compact distributed model topology consisting of two cascaded π sections (double-π network topology [10]–[12]) is utilized, as illustrated in Fig. 3. The corresponding distributed double-π equivalent-circuit model also incorporates transformer loops to accurately model series loss effects over a wide frequency range.

Both single- and double-π compact wide-band models consist entirely of ideal lumped elements. The component values are determined from measured two-port S-parameter data using a robust automated extraction procedure based on a least squares (LS) fitting algorithm [7] and a scaling technique for the double-π model. To verify the capabilities and demonstrate the strengths of the new modeling methodology, a number of sample spiral inductors covering the common classes of on-chip spiral inductors are extracted from measurement data.

TABLE I
GENERAL CLASSIFICATIONS OF SPIRAL INDUCTORS

	Inductor Type				Modeled Effects			
	Electrical Size		Substrate Loss		Prox-	Skin	Substrate	Distributed
	Small	Large	Low	High	imity		Eddy Current	
1	•		•		◇	◇		
2	•			•	◇	◇	◇	
3		•	•		◇	◇		◇
4		•		•	◇	◇	◇	◇

II. MODELING METHODOLOGY

The primary focus of this paper is to set forth a modeling methodology that can be employed to accurately characterize a wide variety of spiral inductors. In general, spiral inductors on a silicon substrate may be classified into four categories, as shown in Table I. A number of modeling techniques are currently available to handle categories 1 and 2 [2], [8], [9], [13]. The more challenging spirals to model are contained within categories 3 and 4. The difficulties in capturing the distributed trends in spiral inductors have recently been addressed in [10], [11], and [14]. Here, a methodology is presented that encompasses all four general categories outlined above in one comprehensive modeling methodology. Combining the single- and double-π network topologies along with a fast automated extraction procedure produces a comprehensive wide-band modeling methodology that can accurately model the common classes of spiral inductors used in modern silicon-based RF integrated circuits (RFICs).

The modeling methodology can be divided into two general steps. The first step is to develop a network topology whose frequency-dependent branch impedance and admittances can be determined from given two-port measurement S-parameters. Furthermore, the resulting frequency-dependent network branch admittances and impedances, such as $Z_{\text{series}}(\omega)$ and $Y_{\text{shunt}_k}(\omega)$, shown in Figs. 2 and 3, should be synthesizable in terms of ideal lumped-element circuits including parameter extraction within an automated procedure. In this paper, the single- and double-π network topologies, shown in Figs. 2 and 3, are employed. The three branch elements in the single-π model (Fig. 2) can be directly (uniquely) expressed in terms of the three independent two-port S- or Y-parameters of the spiral inductor [15]. The double-π network, shown in Fig. 3, however, has four unknown branch functions. A fourth relationship based on a scaling technique is formulated in Section IV-B.

The second step of the modeling methodology is to represent each network branch in terms of an ideal lumped-element circuit and extract the component values. To simplify this process and avoid the need for extracting complex poles, the network branches are limited to either G, C or R, L circuits based upon the physical effects they are representing. The series network branch $Z_{\text{series}}(\omega)$ is used to model the frequency-dependent resistive and inductive component of the inductor, including higher order loss effects. To model the frequency dependence of the series branches, transformer loops are utilized, as in [4]. The transformer loops model the effects of the frequency-dependent series loss in the spiral inductor, which can be attributed to conductor skin effect, proximity effect, and substrate eddy-current

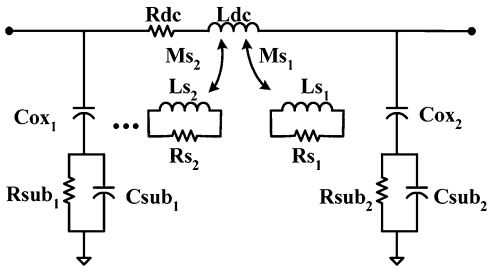

Fig. 4. Wide-band compact equivalent-circuit model for spiral inductors in RFICs in a single-π topology.

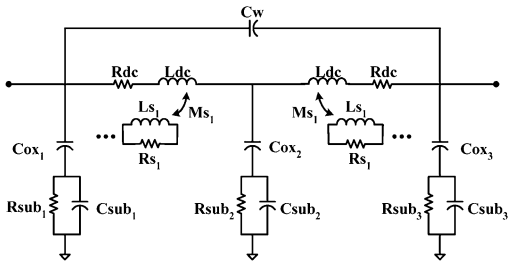

Fig. 5. Wide-band distributed equivalent-circuit model for spiral inductors in RFICs.

loss for low-resistivity substrates [8], [9]. The shunt network branches $Y_{\mathrm{shunt}_k}(\omega)$ are utilized to model the electrical interactions of the metal windings with the Si–SiO_2 multilayer substrate, as presented in [2] and [13]. Care must be taken to choose ideal lumped-element circuits that not only accurately model the frequency-dependent branch impedance $Z_{\mathrm{series}}(\omega)$ and branch admittances $Y_{\mathrm{shunt}_k}(\omega)$, but are also feasible in the implementation of an automated extraction procedure.

III. Equivalent-Circuit Models

A. Single-π Equivalent-Circuit Model

Fig. 4 shows the wide-band single-π equivalent-circuit model for spiral inductors. The inductance L_{dc} and resistance R_{dc} in the series branch represent the spiral inductor's series resistance and inductance at the low-frequency limit, respectively. The inductance L_{s_i} and resistance R_{s_i} simulate the ith transformer loop to account for the frequency-dependent losses. The mutual inductances M_{s_i} between L_{s_i} and L_{dc} can be thought of partly representing the inductive coupling between the spiral metallization and semiconducting substrate. The impedance of the series branch with transformer loops is given by [4]

$$Z_{\mathrm{series}}(\omega) = R_{\mathrm{dc}} + j\omega L_{\mathrm{dc}} - \sum_{i=1}^{N} \frac{M_{s_i}^2 (j\omega)^2}{R_{s_i} + j\omega L_{s_i}} \tag{2}$$

where N is the number of transformer loops. With only a single loop, the series circuit is effectively a simple transformer with a resistive load. Each additional transformer loop adds an extra term to the summation in (2), which allows for more variability in the frequency response. In (2), the element L_{s_i} is arbitrarily chosen as 1 μH to uniquely determine the equation (see Section IV-C). It should also be pointed out that there is no interwinding capacitance connecting ports 1 and 2, as is commonly used in the nine-element model. The interwinding capacitance is used to model an increase in effective $L_{12}(\omega)$ at higher frequencies; however, distributed trends will be present and pronounced at lower frequencies, resulting in the need for a double-π model. The double-π model described in Section III-B includes an interwinding capacitance.

The standard C–G/C topology consisting of ideal G and C elements is used for the shunt branches in the π configuration of the wide-band compact model. Increased flexibility can be realized by adding one or more parallel G/C combinations in series with the basic C–G/C circuit. The impedance of this augmented shunt circuit is

$$\frac{1}{Y_{\mathrm{shunt}_k}(\omega)} = \frac{1}{j\omega C_{\mathrm{ox}_k}} + \sum_{i=1}^{N} \frac{1}{G_{\mathrm{sub}_{k,i}} + j\omega C_{\mathrm{sub}_{k,i}}} \tag{3}$$

where N is the total number of G/C combinations in the shunt circuit and k is the branch number.

B. Double-π Equivalent-Circuit Model

To include distributed effects in a compact spiral inductor model, the single-π network topology is extended to an equivalent higher order ladder network. The resulting double-π network model is shown in Fig. 3. The frequency-dependent shunt admittance and series impedance branches can be represented over a wide frequency range by ideal lumped-element circuits, similar to the wide-band equivalent-circuit model in the single-π network topology. The corresponding new wide-band distributed equivalent-circuit model for spiral inductors is shown in Fig. 5. An additional parallel capacitance is added to include the capacitive effects between the metal windings of the spiral inductor. Interwinding capacitance has increased importance when capturing the distributed characteristics of the metal windings. As in the single-π model, the transformer loops represent the frequency-dependent series loss effects in the spiral inductor. The loss mechanisms include conductor skin and proximity effect and the effects of eddy-current loss in the semiconducting substrate. The general trend of these loss mechanisms is an increase in series resistance and a decrease in series inductance with increasing frequency. Distributed effects resulting in a decreasing or negative effective series resistance at higher frequencies are obtained in the new distributed equivalent-circuit model through the interaction of the series branch and center shunt branch circuits. All lumped elements are chosen in such a way as to accurately model the electrical effects and to be compatible with an automated extraction procedure. If this extra precaution is not taken, an accurate equivalent-circuit model can be developed, but an automated extraction procedure may not be feasible.

IV. Extraction Procedure

A. Single-π Equivalent-Circuit Model

The extraction of the single-π equivalent-circuit model begins with the network solution of the single-π network shown

in Fig. 2. The series impedance can be directly obtained from the Y_{12} admittance parameter, as previously shown in (1). The two shunt branches shown in Fig. 2 are extracted as

$$Y_{\text{shunt}_1}(\omega) = Y_{11}(\omega) + Y_{12}(\omega) \tag{4}$$

$$Y_{\text{shunt}_2}(\omega) = Y_{22}(\omega) + Y_{12}(\omega). \tag{5}$$

The circuit element extraction using Cauchy's method, as described in Section IV-C, is performed for the series branch $Z_{\text{series}}(\omega)$ and the two shunt branches $Y_{\text{shunt}_1}(\omega)$ and $Y_{\text{shunt}_2}(\omega)$.

B. Double-π Equivalent-Circuit Model

The extraction of the double-π equivalent-circuit model begins with the network solution of the double-π network shown in Fig. 3. The given inductor measurements provide three independent two-port network parameters $Y_{11}m$, $Y_{12}m$ and $Y_{22}m$. It should be pointed out that the interwinding capacitance extraction is trivial and is not shown explicitly in the network topology in Fig. 3. Extraction of the interwinding capacitance is done with high-frequency data and removed from the measured short-circuit admittance parameters as

$$Y_{11}(\omega) = Y_{11m}(\omega) - j\omega C_w \tag{6}$$

$$Y_{12}(\omega) = Y_{12m}(\omega) + j\omega C_w \tag{7}$$

$$Y_{22}(\omega) = Y_{22m}(\omega) - j\omega C_w. \tag{8}$$

These three modified independent network parameters are used in the following extraction process. The four unknown network branches $Z_{\text{series}}(\omega)$, $Y_{\text{shunt}_1}(\omega)$, $Y_{\text{shunt}_2}(\omega)$, and $Y_{\text{shunt}_3}(\omega)$ of the double-π network shown in Fig. 3 are related to the three independent network parameters as

$$Y_{11}(\omega) = Y_{\text{shunt}_1}(\omega) + \frac{\frac{1}{Z_{\text{series}}(\omega)}\left(Y_{\text{shunt}_2}(\omega) + \frac{1}{Z_{\text{series}}(\omega)}\right)}{Y_{\text{shunt}_2}(\omega) + \frac{2}{Z_{\text{series}}(\omega)}} \tag{9}$$

$$Y_{12}(\omega) = -\frac{\left(\frac{1}{Z_{\text{series}}(\omega)}\right)^2}{Y_{\text{shunt}_2}(\omega) + \frac{2}{Z_{\text{series}}(\omega)}} \tag{10}$$

$$Y_{22}(\omega) = Y_{\text{shunt}_3}(\omega) + \frac{\frac{1}{Z_{\text{series}}(\omega)}\left(Y_{\text{shunt}_2}(\omega) + \frac{1}{Z_{\text{series}}(\omega)}\right)}{Y_{\text{shunt}_2}(\omega) + \frac{2}{Z_{\text{series}}(\omega)}}. \tag{11}$$

Unlike the case of a single-π network, the four network branches cannot be uniquely determined from the three independent network parameters. To solve the network, a frequency-dependent complex scaling relationship between two shunt branches

$$Y_{\text{shunt}_2}(\omega) = \xi(\omega) Y_{\text{shunt}_1}(\omega) \tag{12}$$

is defined. The specification of the complex scaling function $\xi(\omega)$ is achieved simply in terms of three real scaling constants, as described in the Appendix. Equations (9)–(11) together with the scaling relationship (12) result in the following polynomial equation for series branch impedance function $Z_{\text{series}}(\omega)$:

$$\frac{1}{Y_{12}(\omega)}\left(\frac{1}{Z_{\text{series}}(\omega)}\right)^2 + \big(2 - \xi(\omega)\big)\frac{1}{Z_{\text{series}}(\omega)} + \xi(\omega)\big(Y_{11}(\omega) - Y_{12}(\omega)\big) = 0. \tag{13}$$

Although the polynomial needs to be solved for every frequency point, the polynomial solution is desirable because it is computationally very fast. With $Z_{\text{series}}(\omega)$ determined, the three shunt admittance branches are found as

$$Y_{\text{shunt}_1}(\omega) = Y_{11}(\omega) - Y_{12}(\omega) - \frac{1}{Z_{\text{series}}(\omega)} \tag{14}$$

$$Y_{\text{shunt}_2}(\omega) = \xi(\omega) Y_{\text{shunt}_1}(\omega) \tag{15}$$

$$Y_{\text{shunt}_3}(\omega) = Y_{22}(\omega) - Y_{12}(\omega) - \frac{1}{Z_{\text{series}}(\omega)}. \tag{16}$$

As a final step, a circuit element extraction using Cauchy's method, as described in Section IV-C, is performed for the series branch $Z_{\text{series}}(\omega)$ and the three shunt branches $Y_{\text{shunt}_1}(\omega)$, $Y_{\text{shunt}_2}(\omega)$, and $Y_{\text{shunt}_3}(\omega)$.

C. Circuit Element Extraction

An important consideration in developing compact models is the need for a fast and accurate means of extracting the component values. Typically, compact models, including the nine-element model, are extracted using time-consuming optimization. Since optimizers involve an iterative solution process, they can be prone to convergence problems, depending on the initial values supplied by the user. The optimizer may converge to a "local minimum" or possibly never reach convergence. To avoid these problems with the more complex transformer loop model, we have developed a robust computer-aided design (CAD)-oriented extraction methodology using an LS fitting procedure. Due to the large number of frequency points and limited number of components, the LS fitting procedure involves the solution of an overdetermined system of equations. Note that this extraction approach is feasible because of the simple mapping between the coefficients of the resulting rational polynomial and the component values in the wide-band compact model, as illustrated at the conclusion of this section.

As (2) and (3) show, both the series and shunt impedance functions include summations of single-pole terms, which can be rewritten as rational polynomials of $j\omega$. To take advantage of the rational polynomial form, Cauchy's method [7], [16] is used to extract the coefficients of the rational polynomial and, hence, component values involved in the summations. To illustrate the extraction procedure, the main steps in the extraction are described for the series impedance branch. The shunt circuit extraction is similar and the main differences will be described.

Investigation of the series impedance function shows that, at low frequencies, R_{dc} and L_{dc} dominate the impedance of the series circuit in the transformer loop model. The dc values can be found by separating the measured data, similar to (1), into the

resistive and inductive parts, and extracting the low-frequency asymptotes of both curves. After obtaining $R_{\rm dc}$ and $L_{\rm dc}$, the remaining unknowns are isolated by rearranging (2) as

$$T(jw) =: \frac{R_{\rm dc} + j\omega L_{\rm dc} - Z_{\rm series}(\omega)}{(j\omega)^2} = \sum_{i=1}^{N} \frac{M_{s_i}^2}{R_{s_i} + j\omega L_{s_i}}. \tag{17}$$

Equation (17) shows that the only remaining terms are due to the transformer loops and are contained in a summation of single-pole functions. This summation can be rewritten as a rational polynomial in $j\omega$

$$T(jw) = \frac{a_0 + a_1(\omega) + \cdots + a_{n-1}(j\omega)^{n-1}}{b_0 + b_1(j\omega) + \cdots + b_n(j\omega)^n} = \frac{N(j\omega)}{D(j\omega)}. \tag{18}$$

Rewriting (18) and applying it to each frequency point ω_m ($m = 1, 2, \ldots, M$) results in a set of M complex equations of the form

$$T(j\omega_m) \cdot D(j\omega_m) - N(j\omega_m) = 0. \tag{19}$$

The total number of coefficients in the rational polynomial is three or five for the single and double transformer-loop models, respectively, while the number of frequency points is on the order of 100 for the examples shown in this paper. The example of the commonly used single transformer-loop case can be used to clarify the process. The set of M complex equations in (19) is rewritten as

$$T(j\omega_m) \cdot \left[b_0 + b_1(j\omega)\right] - a_0 = 0 \tag{20}$$

which must be satisfied at each frequency point of interest. The resulting overdetermined system is solved directly using a standard matrix eigenvalue equation approach. The components of the resulting eigenvalue vector provide the coefficients of the rational polynomial set forth in (18). A partial fraction expansion is performed on the rational polynomial to obtain the poles and residues written, in general, as

$$\frac{N(j\omega)}{D(j\omega)} = \frac{r_1}{(j\omega) - p_1} + \cdots + \frac{r_n}{(j\omega) - p_n}. \tag{21}$$

In the case of the single transformer loop, the simple mapping function is used to map (17) to the poles and residues of (21) as

$$\frac{r_0}{(j\omega) - p_0} = \frac{\dfrac{M_{si}^2}{L_{si}}}{(j\omega) + \dfrac{R_{si}}{L_{si}}} \tag{22}$$

where L_{si} is taken as a scaling factor and, as previously mentioned, has been chosen as 1 μH for all models presented in this paper. This value of L_{si} can be chosen arbitrarily, but it should be taken into consideration that $R_{si} \propto L_{si}$ and $M_{si} \propto \sqrt{L_{si}}$. The occurrence of a successful extraction will not be dependent on the arbitrarily chosen value of L_{si}.

The impedance function of the shunt circuits is similar in form to that of the series branch circuit, as can be seen from (3). $C_{\rm ox}$ can be extracted from the low-frequency asymptote of the shunt impedance, and the impedance function is rearranged as

$$\frac{1}{Y_{{\rm shunt}_k}(\omega)} - \frac{1}{j\omega C_{{\rm ox}_k}} = \sum_{i=1}^{N} \frac{1}{G_{{\rm sub}_{k,i}} + j\omega C_{{\rm sub}_{k,i}}}. \tag{23}$$

This form directly leads to an extraction using Cauchy's method, as explained above, where only the simple mapping of poles and residues to the impedance function (23) must be rearranged. In the commonly used C–G/C equivalent shunt circuit, the simple mapping is arranged with (23) as

$$\frac{r_0}{(j\omega) - p_0} = \frac{\dfrac{1}{C_{{\rm sub}_{k,1}}}}{(j\omega) + \dfrac{G_{{\rm sub}_{k,1}}}{C_{{\rm sub}_{k,1}}}}. \tag{24}$$

In a similar manner, the mappings of C–G/C–G/C as well as double transformer loops are arranged. Caution must be given to the generation of the poles and residues indicated in (21), which can result in irrational polynomials due to measurement noise [17].

Due to the similarities in the impedance functions of the series and shunt circuits of the wide-band compact model, the same algorithm can be used to extract all branches of the equivalent-circuit model, which leads to a very compact and efficient extraction procedure. The extraction time for a typical complete equivalent-circuit model consisting of single or double transformer loops and C–G/C or C–G/C–G/C shunt circuits typically is on the order of 30 s for the single-π equivalent-circuit model and 90 s for the double-π equivalent-circuit model on a SPARC Ultra10 workstation.

TABLE II
DESCRIPTIONS OF SPIRAL INDUCTORS USED FOR MODELING RESULTS

Inductor	Approximate Inductance	Substrate Resistivity	Epi Layer Resisitivity	Electrical Size
A	1.5 nH	10 Ω-cm	-	Small
B	1.5 nH	0.01 Ω-cm	10 Ω-cm	Small
C	9.5 nH	10 Ω-cm	-	Large
D	4.5 nH	0.01 Ω-cm	10 Ω-cm	Large

V. RESULTS

To demonstrate the broad capabilities of the presented comprehensive modeling methodology, four inductors from the four general classes of spiral inductors were modeled. The inductors were chosen to show the flexibility of the modeling methodology to accurately characterize a broad class of inductors. A brief description of the inductors is contained in Table II. All inductors were fabricated in BiCMOS processes with or without an epi-layer. Inductor *B* was modeled with the single-π equivalent-circuit model. The remaining inductors were modeled with the double-π equivalent-circuit model for maximum accuracy over the frequency range of 0.1 to 10 GHz. In order to demonstrate the benefits of modeling electrically large inductors with the double-π model, single-π models were also extracted for comparison purposes for inductors *C* and *D*. To illustrate the

TABLE III
EXTRACTED SINGLE-π EQUIVALENT-CIRCUIT PARAMETERS FOR A 1.5-nH SPIRAL

Parameters	Single Loop Model	Double Loop Model	Parameters	Both Models
R_{DC}	2.3086 Ω	2.334 Ω	C_{ox_1}	67.23 fF
L_{DC}	1.408 nH	1.494 nH	$C_{sub_{1,1}}$	199.05 fF
R_{s_1}	33785 Ω	53435 Ω	$G_{sub_{1,1}}$	10.39 mS
L_{s_1}	1 μH	1 μH	C_{ox_2}	76.81 fF
M_{s_1}	17.20 nH	16.07 nH	$C_{sub_{2,1}}$	267.0 fF
R_{s_2}	-	4955.0 Ω	$G_{sub_{2,1}}$	10.66 mS
L_{s_2}	-	1 μH	-	-
M_{s_2}	-	10.97 nH	-	-

TABLE IV
EXTRACTED DOUBLE-π EQUIVALENT-CIRCUIT PARAMETERS FOR A 9.5-nH SPIRAL

Parameters	Extracted Values
R_{DC}	2.778 Ω
L_{DC}	4.325 nH
R_{s_1}	26.0 $k\Omega$
L_{s_1}	1 μH
M_{s_1}	13.61 nH
C_w	10.00 fF
C_{ox_1}	19.71 fF
$C_{sub_{1,1}}$	64.67 fF
$G_{sub_{1,1}}$	9.90 mS
C_{ox_2}	73.01 fF
$C_{sub_{2,1}}$	10.82 fF
$G_{sub_{2,1}}$	2.189 mS
C_{ox_3}	15.27 fF
$C_{sub_{3,1}}$	31.06 fF
$G_{sub_{3,1}}$	1.688 mS

two possible outputs of an extraction process, sample results are shown for the single-π and double-π equivalent circuits. Table III lists the circuit component values of the single-π model for inductor *B* obtained with the automated extraction procedure. Table IV lists the double-π extracted circuit component values obtained for inductor *C*.

To demonstrate the accuracy of the models, a number of inductor characteristics that are of importance to the circuit designer are shown. Fig. 6 shows the short-circuit input resistance R_{11} and short-circuit input inductance L_{11} for inductors *A* and *B*, as defined by

$$\frac{1}{Y_{11}(\omega)} = R_{11}(\omega) + j\omega L_{11}(\omega). \tag{25}$$

There is slight improvement in modeling performance for inductor *B* above 8 GHz by using two transformer loops. Similarly, the $R_{11}(\omega)$ results for inductors *C* and *D* are shown in Fig. 7. The model results for $L_{11}(\omega)$ are shown in Fig. 8 for inductors *A* and *B* and in Fig. 9 for inductors *C* and *D*, respectively. These results demonstrate the accuracy of the modeling methodology in terms of the one-port characteristics of the spiral inductors.

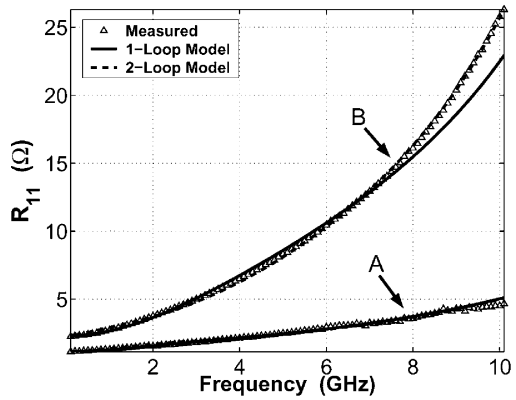

Fig. 6. Input resistance $R_{11}(\omega)$ for inductors *A* (double-π model) and *B* (single-π model) obtained from measurements and modeled using the comprehensive modeling methodology.

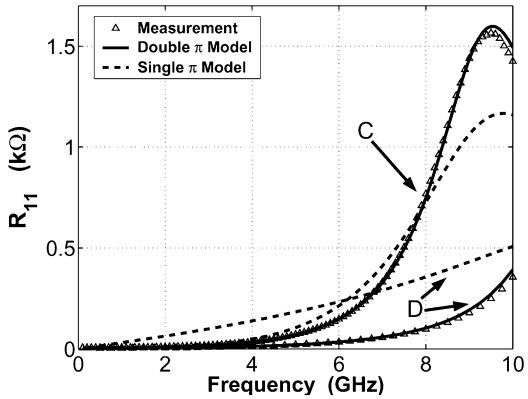

Fig. 7. Input resistance $R_{11}(\omega)$ for inductors *C* and *D* obtained from measurements and modeled using the comprehensive modeling methodology using single transformer loops.

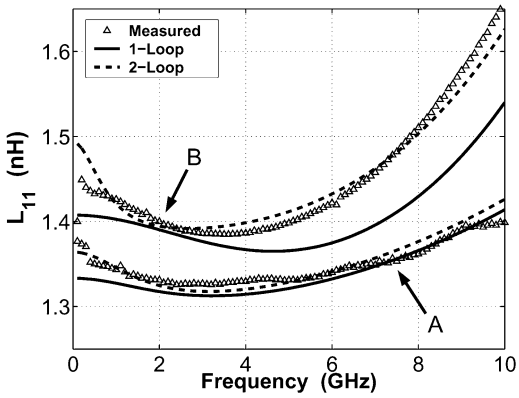

Fig. 8. Input inductance $L_{11}(\omega)$ for inductors *A* (double-π model) and *B* (single-π model) obtained from measurements and modeled using the comprehensive modeling methodology.

The second set of characteristics to show are the mutual resistance R_{12} and mutual inductance L_{12}, defined by (1). The model results for $R_{12}(\omega)$ are presented in Fig. 10 for inductors *A* and *B* and in Fig. 11 for inductors *C* and *D*, respectively. The results for $R_{12}(\omega)$ are the best indicator for the need of a distributed model. A single-π model is unable to capture the negative-resistance trends seen in $R_{12}(\omega)$ at higher frequencies. When using a dis-

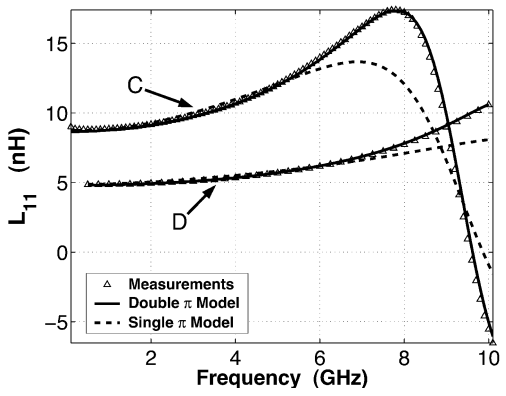

Fig. 9. Input inductance $L_{11}(\omega)$ for inductors *C* and *D* obtained from measurements and modeled using the comprehensive modeling methodology using single transformer loops.

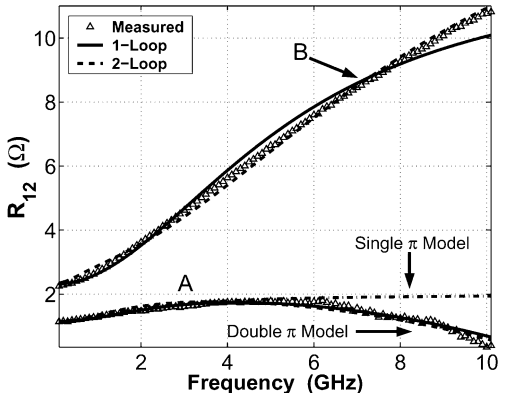

Fig. 10. Resistance $R_{12}(\omega)$ for inductors *A* (double-π model) and *B* (single-π model) obtained from measurements and modeled using the comprehensive modeling methodology.

tributed model, the series resistance parameter is able to achieve negative values because of the presence of the additional shunt C–G/C branch at the center. Inductor *A* is a borderline case for the necessity of using a double-π model. The single-π model is able to model the inductor accurately up to 6 GHz. To demonstrate the modeling capabilities of the single-π model prior to decreases in $R_{12}(\omega)$, a single-π model using double transformer loops was extracted for inductor *A* with measurement data up to 6 GHz. The results shown in Fig. 10 illustrate the accuracy of the single-π model before diverging from measurement data beyond 6 GHz. Comparisons of the model results for $L_{12}(\omega)$ are shown in Fig. 12 for inductors *A* and *B* and Fig. 13 for inductors *C* and *D*, respectively.

The last performance characteristic is the input quality factor $Q_{11}(\omega)$ defined as

$$Q_{11}(\omega) = \frac{\mathrm{Im}\left(\dfrac{1}{Y_{11}(\omega)}\right)}{\mathrm{Re}\left(\dfrac{1}{Y_{11}(\omega)}\right)}. \tag{26}$$

The input quality factor is an overall performance measure of a spiral inductor. To show the flexibility of the modeling methodology in accurately capturing the overall performance of a wide variety of spiral inductors, the results for $Q_{11}(\omega)$ are shown in a

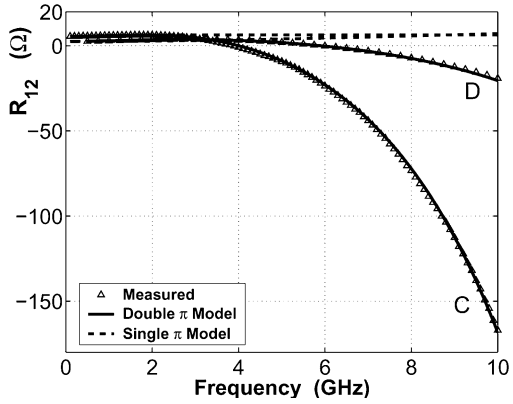

Fig. 11. Resistance $R_{12}(\omega)$ for inductors *C* and *D* obtained from measurements and modeled using the comprehensive modeling methodology using single transformer loops.

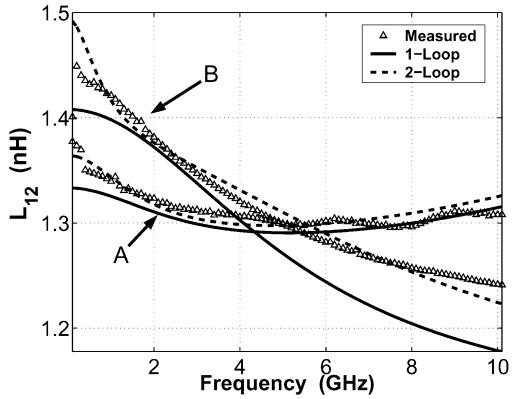

Fig. 12. Inductance $L_{12}(\omega)$ for inductors *A* (double-π model) and *B* (single-π model) obtained from measurements and modeled using the comprehensive modeling methodology.

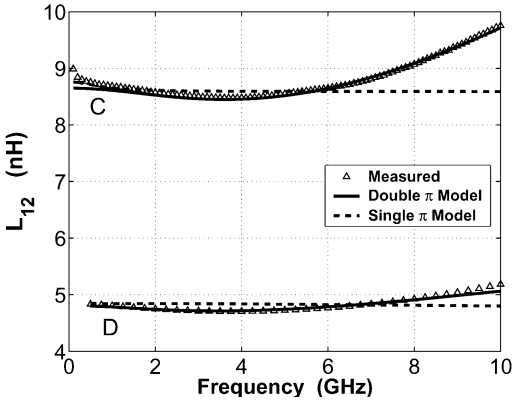

Fig. 13. Inductance $L_{12}(\omega)$ for inductors *C* and *D* obtained from measurements and modeled using the comprehensive modeling methodology using single transformer loops.

single diagram in Fig. 14. All four models show excellent agreement over the entire frequency range from 0.1 to 10 GHz. In particular, all models give accurate peak Q information.

To allow for further comparison of modeled and measured data, an S-parameter comparison is shown for inductor *C*. The modeled S-parameters $S_{11}(\omega)$ and $S_{12}(\omega)$ are shown in comparison with measurement data in Fig. 15 for inductor *C*. There is excellent accuracy over the entire frequency range for the modeled S-parameters. This comparison illustrates the benefits

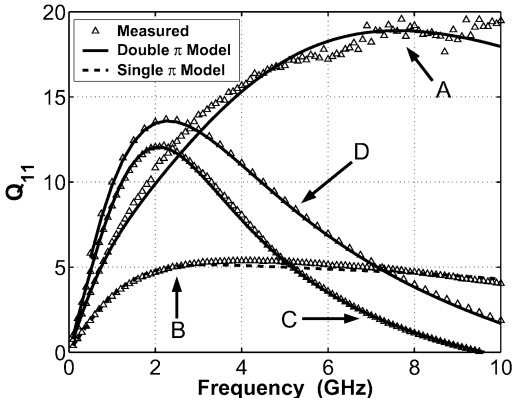

Fig. 14. Input quality factor $Q_{11}(\omega)$ for inductors *A–D* obtained from measurements and modeled using the comprehensive modeling methodology. (Inductors A and B are modeled using two transformer loops, inductors C and D are modeled using one transformer loop.)

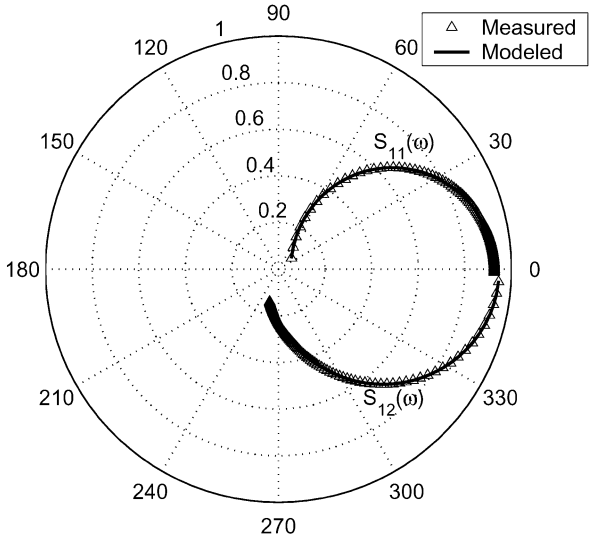

Fig. 15. Comparison of modeled and measured S-parameters $S_{11}(\omega)$ and $S_{12}(\omega)$ for inductor *C*.

of using the R, L, Q characteristics for viewing the otherwise undetectable inaccuracies. In addition to the results shown here, a large number of other spirals from the four categories have been modeled, and similar excellent model performance was observed [18].

VI. Conclusion

A new comprehensive methodology for wide-band compact modeling of spiral inductors on lossy silicon substrate has been presented. The modeling methodology consists of both wide-band compact equivalent-circuit models and an automated extraction procedure. Distributed effects in electrically larger spirals are modeled in terms of a double-π equivalent-circuit topology. The frequency dependence in the equivalent series resistance and series inductance of the spiral inductor is modeled in terms of coupled transformer loops, which capture higher order loss effects, including conductor skin and proximity effects and the effects of eddy-current loss in the semiconducting substrate. The automated extraction procedure is based on Cauchy's method and takes advantage of the simple mapping between the coefficients of the rational impedance functions and the equivalent-circuit elements. The extraction process is considerably faster in comparison with standard optimization techniques.

To verify the accuracy of the new methodology, a set of four inductors was extracted from two-port S-parameter measurements over the frequency range of 0.1–10 GHz. The four inductors were chosen to cover four general classes of spiral inductors on lossy silicon substrate. Results for several significant characteristics $R_{11}(\omega)$, $L_{11}(\omega)$, $R_{12}(\omega)$, $L_{12}(\omega)$, $Q_{11}(\omega)$, $S_{11}(\omega)$, and $S_{12}(\omega)$ were presented. The excellent accuracy of the results across all classes of spiral inductors demonstrates the flexibility of the modeling methodology. The new methodology for wide-band compact-model development for spiral inductors should be very useful in the design of RFICs and mixed-signal ICs. The methodology produces an equivalent circuit with ideal lumped elements allowing for direct implementation of the model in common circuit simulators such as SPICE for transient and frequency-domain simulation.

Appendix

The scaling relationship (12) needed for the network solution of the double-π network is obtained by simply using real constants κ_1, κ_2, and κ_3 within a limited range that can be quickly scanned. Typical ranges used for this paper were $1 \leq \kappa_1 \leq 10$, $1 \leq \kappa_2 \leq 10$, and $0.5 \leq \kappa_3 \leq 1$. First, an initial estimate for shunt admittance $Y_{\text{shunt}_1}(\omega)$ using the single-π network model in Fig. 2 is obtained. The extraction of a C–G/C circuit is used to produce rough estimates for the equivalent-circuit parameters C_{ox_e}, G_{sub_e}, and C_{sub_e}. The estimated shunt branch is given in terms of the equivalent-circuit parameters as

$$Y_{\text{estimate}}(\omega) = \frac{j\omega C_{\text{ox}_e}(G_{\text{sub}_e} + j\omega C_{\text{sub}_e})}{G_{\text{sub}_e} + j\omega(C_{\text{ox}_e} + C_{\text{sub}_e})}. \tag{27}$$

Scaling of each extracted value is performed using κ_1, κ_2, and κ_3 to obtain $\kappa_1 C_{\text{ox}_e}$, $\kappa_2 G_{\text{sub}_e}$, and $\kappa_3 C_{\text{sub}_e}$ with

$$Y_{\kappa\ \text{scaled}}(\omega) = \frac{j\omega\kappa_1 C_{\text{ox}_e}(\kappa_2 G_{\text{sub}_e} + j\omega\kappa_3 C_{\text{sub}_e})}{\kappa_2 G_{\text{sub}_e} + j\omega(\kappa_1 C_{\text{ox}_e} + \kappa_3 C_{\text{sub}_e})}. \tag{28}$$

The two resulting C–G/C admittances are used for the creation of a frequency-dependent scaling factor given as

$$\xi(\omega) = \kappa_1 \frac{(\kappa_2 G_{\text{sub}_e} + j\kappa_3\omega C_{\text{sub}_e})\left(G_{\text{sub}_e} + j\omega(C_{\text{ox}_e} + C_{\text{sub}_e})\right)}{(G_{\text{sub}_e} + j\omega C_{\text{sub}_e})\left(\kappa_2 G_{\text{sub}_e} + j\omega(\kappa_1 C_{\text{ox}_e} + \kappa_3 C_{\text{sub}_e})\right)}. \tag{29}$$

References

[1] R. L. Brown and W. R. Smith, "Embedded passive functions for RF and mixed-signals circuits," presented at the Multichip Module Conf., 1997.

[2] J. R. Long and M. A. Copeland, "The modeling, design, and characterization of monolithic inductors for silicon RF IC's," *IEEE J. Solid-State Circuits*, vol. 32, pp. 357–368, Mar. 1997.

[3] S. S. Mohan, M. d. M. Hershensen, S. P. Boyd, and T. H. Lee, "Simple accurate expressions for planar spiral inductors," *IEEE J. Solid-State Circuits*, vol. 34, pp. 1419–1424, Oct. 1999.

[4] J. Zheng, Y.-C. Hahm, V. K. Tripathi, and A. Weisshaar, "CAD-oriented equivalent circuit modeling of on-chip interconnects on lossy silicon substrate," *IEEE Trans. Microwave Theory Tech.*, vol. 48, pp. 1443–1451, Sept. 2000.

[5] J. Zheng, V. K. Tripathi, and A. Weisshaar, "Characterization and modeling of multiple coupled on-chip interconnects on silicon substrate," *IEEE Trans. Microwave Theory Tech.*, vol. 49, pp. 1733–1739, Oct. 2001.
[6] W. B. Kuhn and N. K. Yanduru, "Spiral inductor substrate loss modeling in silicon RFICs," in *Proc. IEEE RAWCON*, 1998, pp. 305–308.
[7] E. C. Levy, "Complex-curve fitting," *IRE Trans. Automat. Contr.*, vol. 4, pp. 37–43, May 1959.
[8] D. Melendy, P. Francis, C. Pichler, K. Hwang, G. Srinivasan, and A. Weisshaar, "Wide band compact modeling of spiral inductors in RFICs," in *IEEE MTT-S Int. Microwave Symp. Dig.*, June 2002, pp. 717–720.
[9] ——, "A new wide-band compact model for spiral inductors in RFICs," *IEEE Electron Device Lett.*, vol. 23, pp. 273–275, May 2002.
[10] A. Watson, P. Francis, K. Hwang, and A. Weisshaar, "Wide-band distributed modeling of spiral inductors in RFICs," in *IEEE MTT-S Int. Microwave Symp. Dig.*, June 2003, pp. 1011–1014.
[11] Y. Cao, R. A. Groves, X. Huang, N. D. Zamdmer, J.-O. Plouchart, R. A. Wachnik, T.-J. King, and C. Hu, "Frequency-independent equivalent-circuit model for on-chip spiral inductors," *IEEE J. Solid-State Circuits*, vol. 38, pp. 419–426, Mar. 2003.
[12] T. Kamgaing, T. Myers, M. Petras, and M. Miller, "Modeling of frequency dependent losses in two-port and three-port inductors on silicon," in *IEEE MTT-S Int. Microwave Symp. Dig.*, June 2002, pp. 153–156.
[13] J. N. Burghartz, D. C. Edelstein, K. A. Jenkins, and Y. H. Kwark, "Spiral inductors and transmission lines in silicon technology using copper-damascene interconnects and low-loss substrates," *IEEE Trans. Microwave Theory Tech.*, vol. 45, pp. 1961–1968, Oct. 1997.
[14] Y. Cao, R. A. Groves, N. D. Zamdmer, J.-O. Plouchart, R. A. Wachnik, X. Huang, T.-J. King, and C. Hu, "Frequency-independent equivalent circuit model for on-chip spiral inductors," in *Proc. IEEE Custom Integrated Circuits Conf.*, May 2002, pp. 217–220.
[15] D. M. Pozar, *Microwave Engineering*, 2nd ed. New York: Wiley, 1998.
[16] M. Elzinga, K. Virga, L. Zhao, and J. L. Prince, "Pole-residue formulation for transient simulation of high-frequency interconnects using householder LS curve-fitting techniques," *IEEE Trans. Adv. Packag.*, vol. 25, pp. 142–147, May 2000.
[17] D. Melendy, "Modeling of on-chip spiral inductors for silicon RFICs," M.S. thesis, Dept. Elect. Comput. Eng., Oregon State Univ., Corvallis, OR, 2002.
[18] A. Watson, "Analysis and modeling of single-ended and differential spiral inductors in silicon-based RFICs," M.S. thesis, Dept. Elect. Eng. Comput. Sci., Oregon State Univ., Corvallis, OR, 2003.

Adam C. Watson (S'02) was born in Yamhill, OR, in 1979. He received the B.S. degree in applied sciences from George Fox University, Newberg, OR, in 2001, and the B.S. (*magna cum laude*) and M.S. degrees in electrical and electronics engineering from Oregon State University, Corvallis, in 2002 and 2003, respectively.

He was with the Technology Research and Development (TR&D) Group, Maxim Integrated Products, where he developed new package models until 2001. Since that time, he has been involved in a joint research project with the National Semiconductor Corporation, regarding the modeling of inductive passive devices. His current research interests include RF circuit design and CAD modeling.

Daniel Melendy (S'99–M'03) received the B.S. (*magna cum laude*) and M.S. degrees in electrical engineering from Oregon State University, Corvallis, in 2000 and 2002, respectively.

He is currently a Design Engineer with the National Semiconductor Corporation, Federal Way, WA. His current research interests are in the field of RF mixed-signal IC design and scalable compact modeling of on-chip RF passives.

Pascale Francis, photograph and biography not available at time of publication.

Kyuwoon Hwang, photograph and biography not available at time of publication.

Andreas Weisshaar (S'90–M'91–SM'98) received the Diplom-Ingenieur (Dipl.-Ing.) degree in electrical engineering from the University of Stuttgart, Stuttgart, Germany, in 1987, and the M.S. and Ph.D. degrees in electrical and computer engineering from Oregon State University, Corvallis, in 1986 and 1991, respectively.

In 1991, he joined the faculty of the Department of Electrical and Computer Engineering, Oregon State University, and is currently an Associate Professor with the School of Electrical Engineering and Computer Science. He has authored or coauthored over 100 technical papers. He also coauthored *Transmission Lines and Wave Propagation, Fourth Edition* (Boca Raton, FL: CRC Press, 2001). He holds one U.S. patent. His current areas of research include CAD of passive RF and microwave circuits and components, embedded passives, interconnects and electronic packaging, and signal integrity.

Dr. Weisshaar was a guest editor of the IEEE TRANSACTIONS ON MICROWAVE THEORY AND TECHNIQUES December 2002 Symposium Issue. He is currently an associate editor of the IEEE MICROWAVE AND WIRELESS COMPONENTS LETTERS. He serves on the Editorial Board of the IEEE TRANSACTIONS ON MICROWAVE THEORY AND TECHNIQUES and is a member of the Technical Program Committees of several international conferences including the IEEE Microwave Theory and Techniques Society (IEEE MTT-S) International Microwave Symposium (IMS) and the IEEE Topical Meeting on Electrical Performance of Electronic Packaging.